

Comparative study of Al-doped ZnO films deposited by sol-gel and by sputtering using a sintered target from ZnO nanoparticles synthesized by sol-gel

Francisco García-Salinas^a, Alma Vázquez-Durán^{b,*}, José Martín Yáñez-Limón^a

^a Centro de Investigación y de Estudios Avanzados Unidad Querétaro, CINVESTAV, Qro., Querétaro, Mexico

^b Universidad Nacional Autónoma de México-Facultad de Estudios Superiores Cuautitlán, Estado de México, México

ARTICLE INFO

Article history:

Received 12 May 2021

Accepted 15 November 2021

Available online 26 November 2021

Keywords:

Zinc oxide doped films

Sol-gel synthesis

Sputtering

Electrical resistivity

ABSTRACT

Al-doped zinc oxide (ZnO) films were deposited on glass substrates by radio frequency magnetron sputtering using a sintered target of nanoparticles synthesized by sol-gel. The films were characterized using X-ray diffraction, scanning electron microscopy, the four-point probe method for resistivity, energy dispersive X-ray spectroscopy and photoluminescence. The X-ray diffraction patterns showed a hexagonal structure corresponding to the wurtzite phase for all the films, nanoparticles, and sintered targets. The films deposited by sputtering showed a highly preferred orientation to the (002) plane. These films were compared structurally and electrically to those deposited by the sol-gel method. Photoluminescence spectra show a decrease in intensity due to the reduction of defects by the incorporation of Al as dopant in the ZnO films deposited by the both methods (sol-gel and sputtering). The Al-doped ZnO films deposited by sputtering reached resistivity of 0.1 Ω cm and those deposited by sol-gel reached a resistivity of 1.24 Ω cm. The physical properties of these films show potential for application in devices like sensors and biosensors.

© 2021 SECV. Published by Elsevier España, S.L.U. This is an open access article under the CC BY-NC-ND license (<http://creativecommons.org/licenses/by-nc-nd/4.0/>).

Estudio comparativo de películas de ZnO dopadas con Al depositadas mediante sol-gel y erosión catódica usando un blanco sinterizado a partir de nanopartículas de ZnO sintetizadas por sol-gel

RESUMEN

Se depositaron películas de óxido de zinc (ZnO) dopadas con aluminio (Al) sobre sustratos de vidrio mediante erosión catódica de radiofrecuencia usando un blanco sinterizado de nanopartículas sintetizadas por sol-gel. Las películas fueron caracterizadas usando difracción de rayos-X, microscopía electrónica de barrido, método de cuatro puntas para la resistividad, espectroscopía de energía dispersiva de rayos-X y fotoluminiscencia.

Palabras clave:

Películas de ZnO dopadas

Síntesis sol-gel

Erosión catódica

Resistividad eléctrica

* Corresponding author.

E-mail address: almavazquez@comunidad.unam.mx (A. Vázquez-Durán).

<https://doi.org/10.1016/j.bsecv.2021.11.004>

0366-3175/© 2021 SECV. Published by Elsevier España, S.L.U. This is an open access article under the CC BY-NC-ND license (<http://creativecommons.org/licenses/by-nc-nd/4.0/>).

Los patrones de difracción de rayos-X mostraron una estructura hexagonal correspondiente a la fase wurtzita para todas las películas, nanopartículas y blancos sinterizados. Las películas depositadas por erosión catódica mostraron una alta orientación preferencial al plano (002). Estas películas fueron comparadas con las depositadas por el método sol-gel, estructural y eléctricamente. Los espectros de fotoluminiscencia muestran una reducción en intensidad debido a la reducción de defectos por la incorporación de Al como dopante en las películas depositadas por ambos métodos (sol-gel y *sputtering*). Las películas de ZnO dopadas con Al depositadas por erosión catódica alcanzaron resistividades de 0,1 Ω cm y 1,24 Ω cm para las películas de ZnO dopadas con Al depositadas por sol-gel. Las propiedades físicas de estas películas muestran potencial para la aplicación en dispositivos como sensores o biosensores.

© 2021 SECV. Publicado por Elsevier España, S.L.U. Este es un artículo Open Access bajo la licencia CC BY-NC-ND (<http://creativecommons.org/licenses/by-nc-nd/4.0/>).

Introduction

Zinc oxide (ZnO) is an intrinsic n-type semiconductor of the II–VI family; it has a 3.37 eV direct transition band gap and an exciton binding energy of 60 meV at room temperature. ZnO has high transmittance in the visible region. ZnO normally occurs in a hexagonal wurtzite-type structure classified in the P63mc space group with lattice parameters $a = b = 3.249$ Å and $c = 5.2042$ Å with a relationship $c/a = 1.602$ [1–3]. Some of these properties of ZnO can be adjusted by doping. Commonly, ZnO is doped with Gallium (Ga), Indium (In), or Aluminum (Al), which are the elements of group III that are the most used to improve the electrical and optical properties of ZnO. However, the precursors of Ga and In are usually more expensive than the precursors of Al. Consequently, doping with Al may be an alternative for obtaining good physicochemical properties using low doping percentages. Aluminum is an efficient n-type dopant that reduces oxygen vacancy defects; these defects impact the stability of resistivity [2]. Photoluminescence can provide some important information related to the surface defects and oxygen vacancies, and energy levels in semiconductor materials like ZnO. Wang et al. mention that Al incorporation induces changes in energy levels and modify oxygen concentration, so photoluminescence is an adequate technique to analyze the effect of Al as a dopant in ZnO [4].

ZnO is a highly studied material that has different applications. It is used to promote growth in plants when added as nanoparticles [5]. It is used in biomedical applications [6], and as a photocatalyst material [7,8] in devices such as photovoltaic cells, liquid-crystal display (LCD) screens, diodes, ultraviolet (UV) lasers, and sensors [9–15]. ZnO is a convenient material for biosensor design because it can be inexpensive and biocompatible, and it enables devices to have a large surface area, high catalytic capacity, and high electron transfer rate. As a consequence, this material has been used successfully for the detection of glucose, cholesterol, urea, uric acid, vitamins, neurotransmitters, amino acids, captopril [16–19], non-enzymatic glucose sensors [20], and dopamine [21], among others.

ZnO can be synthesized as nanoparticles, thick films, and thin films. However, ZnO films offer the advantage that the material can be recovered easily after use, and they take

advantage of the electrical properties of ZnO on a large scale. The techniques used to deposit ZnO films for application in solar cells, sensors, and other devices are screen printing [22–24], chemical bath [25–27], successive ionic layer adsorption and reaction (SILAR) [28,29], drop-casting [30], sol-gel, and sputtering. The sol-gel technique has the advantage that it can produce thin films with low resistivity and high surface area by adjusting the deposit conditions.

On the other hand, the sputtering technique deposits ZnO films onto substrates directly, without the need for subsequent heat treatment, which facilitates the coating of different surfaces such as polyethylene terephthalate (PET), glass, and quartz without compromising their physicochemical properties, as the obtained films have a highly crystalline quality and low resistivity. Many studies use commercial targets for the sputtering process, or manufacture targets by compressing commercial ZnO and Alumina (Al_2O_3) powders [31–33]; this implies that the doping occurs during the sputtering process. However, some studies use targets synthesized using a chemical process [34], such as sol-gel. These targets have the advantage that during the powder obtention, the doping agent is present inside the lattice before the sputtering process.

In this study, the physicochemical properties of ZnO nanoparticles, and ZnO nanoparticles doped with Al obtained by the sol-gel process were analyzed. In addition, we carried out a comparative study of the structural, electrical and photoluminescence properties of ZnO and ZnO doped with Al (AZO) films deposited on glass, obtained by sol-gel and by sputtering using synthesized targets obtained from the powders derived from the sol-gel process.

Experimental procedure

Materials

The reagents used were zinc acetate dihydrate (ZAD, $\text{Zn}(\text{CH}_3\text{COO})_2 \cdot 2\text{H}_2\text{O}$) of analytical reagent (AR) quality from Sigma–Aldrich (India) and aluminum nitrate nonahydrate ($\text{Al}(\text{NO}_3)_3 \cdot 9\text{H}_2\text{O}$) of AR grade, from Sigma–Aldrich (Germany). Ethanol was used as a solvent. Diethanolamine (DEA, $\text{NH}(\text{C}_2\text{H}_4\text{OH})_2$) was used as a stabilizer.

Synthesis of nanoparticles and target preparation for sputtering

ZAD was added to a solution of DEA and ethanol at 50 °C under stirring, and Al (NO₃)₃·9H₂O was added as the aluminum doping agent. The final solution presented a concentration of 0.5 M of ZAD. DEA was maintained at a molar ratio of 1:1 with respect to ZAD. The concentration of the dopant was fixed at a 1% molar percentage of Al³⁺ with respect to Zn²⁺ (Al³⁺/Zn²⁺). The precursor solution was aged for 10 days and dried at the boiling point until the solvent in the sample was completely evaporated. Subsequently, the product was calcined at 300 °C for 30 min. Thermal treatment was carried out at 500 °C for 1 h to remove the organic remnants and to allow the nanoparticles to completely form.

For the ZnO nanoparticles synthesis, the process and thermal treatment were the same as described above for the AZO nanoparticles, but without adding the doping agent (Al (NO₃)₃·9H₂O).

The resulting nanoparticles powders were pressed using a 2½-in. die with a pressure of 16 MPa and then sintered at 1000 °C for 1 h using a 5 °C/min heating ramp. The sintered target was used to obtain films using radio frequency (RF) magnetron sputtering.

AZO and ZnO films deposited by sputtering

The films were deposited on glass slide substrates (corning slides) using RF magnetron sputtering (Intercovamex V3). The substrates were cleaned with liquid soap, rinsed with distilled water, rinsed with ethanol, and placed in an ultrasonic bath using a mixture of acetone, xylene, and ethanol in a ratio of 1:1:1 by volume for 30 min. Finally, the substrates were rinsed with acetone and dried. The powers used during the deposit were 100 and 150 W, and the power densities were 3.785 W/cm² and 5.677 W/cm², respectively. The substrate temperature was kept constant at room temperature. The argon (Ar) pressure was kept constant at 2 × 10⁻² mbar with a flow of 180 standard cubic centimeters per minute (sccm). The distance between the substrate and the target was maintained at 7 cm. The procedure and parameters for depositing the ZnO and AZO films were the same.

AZO and ZnO films synthesized by sol-gel/dip-coating

ZAD was added to a solution of DEA with ethanol at 50 °C under stirring, and Al (NO₃)₃·9H₂O was added as the doping agent. The final solution was a concentration of 0.5 M ZAD, and DEA was maintained at a molar ratio of 1:1 with ZAD. The concentration of the dopant was fixed at 1% the molar percentage of Al³⁺ with respect to Zn²⁺ (Al³⁺/Zn²⁺). The precursor solution was aged for 10 days, and the films were deposited on glass slide substrates using the dip-coating technique with a withdrawal speed was 6 cm/min, and then dried at 300 °C for 15 min in an air atmosphere. To obtain films with adequate thickness, the dipping-drying process was repeated seven times. Afterward, the films were sintered at 530 °C for 1 h.

ZnO films were deposited using the process and thermal treatment described above for the AZO films, but without adding the doping agent (Al (NO₃)₃·9H₂O).

Characterization techniques

To determine the crystal structure, thin films were characterized by X-ray diffraction using a Rigaku Dmax2100 (Cu Kα radiation, λ = 1.5405 Å) diffractometer. From the X-ray diffraction patterns, the crystallite size was calculated using the Debye-Scherrer equation [35]:

$$D = \frac{k\lambda}{\beta \cos \theta} \quad (1)$$

where k is the Scherrer constant, β is the full width at half maximum (FWHM), λ is the wavelength of the X-rays used, and θ is the angle at which the refraction takes place. This analysis was performed using JADE software and with consideration for the standard Si diffraction pattern in the adjustment of the calibration curve.

Similarly, the texture coefficient (TC_{hkl}) was calculated using the Harris texture equation [35,36]:

$$TC_{hkl} = \frac{I_{hkl}}{IO_{hkl}} \left[\frac{1}{N} \left(\sum_n \frac{I_{hkl}}{IO_{hkl}} \right) \right]^{-1} \quad (2)$$

where I_{hkl} is the experimental intensity, IO_{hkl} is the reference intensity obtained from a powder diffraction file (PDF), and N is the number of planes considered for the analysis.

The morphology of the films was obtained by field emission scanning electron microscopy (FE-SEM) at 1.0 kV for nanoparticles and 2.0 kV for films. The detector was a secondary electron (SE) detector (JEOL 7610F). From the FE-SEM images collected, the size of the grains in the thin films and the particle size of the powders synthesized from sol-gel were determined using ImageJ software, and the results are reported as mean ± standard deviation. The size of the AZO nanoparticles was measured longitudinally. The thickness measurement was carried out using a 3D interference profilometer (optical profilometer, Bruker-Contour GT-InMotion 3D). The resistivity measurement was carried out using the four-point probe method (Loresta-6P equipment, model MCP-T600). The semi-quantitative analysis was carried out with energy dispersive X-ray spectroscopy (EDS) using an environmental scanning electron microscope (ESEM, Philips XL30). Photoluminescence spectra for ZnO and AZO films were measured at room temperature using an LS-55 spectrophotometer (Perkin Elmer, Waltham, MA, USA). The samples were excited at 325 nm and the spectrum was collected in the wavelength range of 350–600 nm.

Results and discussion

AZO nanoparticles and target for sputtering

Fig. 1A shows the X-ray diffraction pattern corresponding to the nanoparticles obtained by the sol-gel method for AZO and ZnO. The patterns agree with the wurtzite phase according to PDF 36-1451, which describes this phase as a hexagonal structure. The average crystallite size for the AZO nanoparticles is 64 nm, and for ZnO, it is 68 nm.

The X-ray diffraction patterns of the sputtering targets are presented in Fig. 1B for AZO and ZnO. In both instances, a

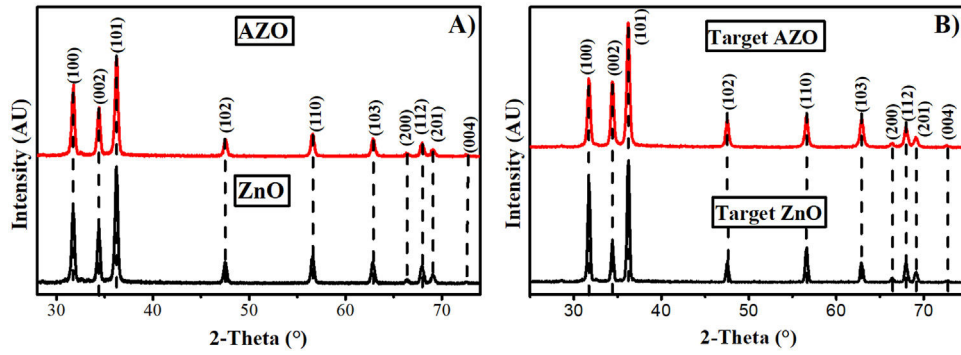


Fig. 1 – X-ray diffraction pattern for (a) ZnO nanoparticles and AZO nanoparticles, (b) AZO target and ZnO target for sputtering.

random orientation agrees with the PDF. The analysis of the X-ray diffraction patterns does not show impurities like aluminum oxide. After pressing and sintering the nanoparticles, the average crystallite size grew to 86 nm for the AZO target, and to more than 100 nm for the ZnO without doping. This increment in crystallite size is due to the diffusion process in the solid or semi-solid state in which sintering is carried out. After the sintering process, the target diameter changed from 6.35 cm (2.5 in) to 5.08 cm (2 in), therefore, the diameter was reduced by 20% for both targets (AZO and ZnO), and the density reached was 93% of the theoretical density for AZO and 95% of that for ZnO (ZnO theoretical density is 5.675 g/cm³ [37]).

In Fig. 2, the FE-SEM images and the size distribution of the synthesized nanoparticles are presented. The FE-SEM images show semispherical particles of ZnO without doping (Fig. 2a) and rod-like particles of AZO (Fig. 2b). In Fig. 2c, the size distribution of ZnO nanoparticles is presented: the mean size is 45 ± 18 nm. In Fig. 2d, the size distribution of the AZO nanoparticles is presented: the mean size is 123 ± 75 nm. The incorporation of Al as dopant during the nanoparticle synthesis modified the morphology and the size distribution, as presented in the figure. The effect of Al on the morphology of AZO nanoparticles has been previously reported by Rameshkumar et al. In their work, they synthesized AZO nanoparticles using the co-precipitation method, and they

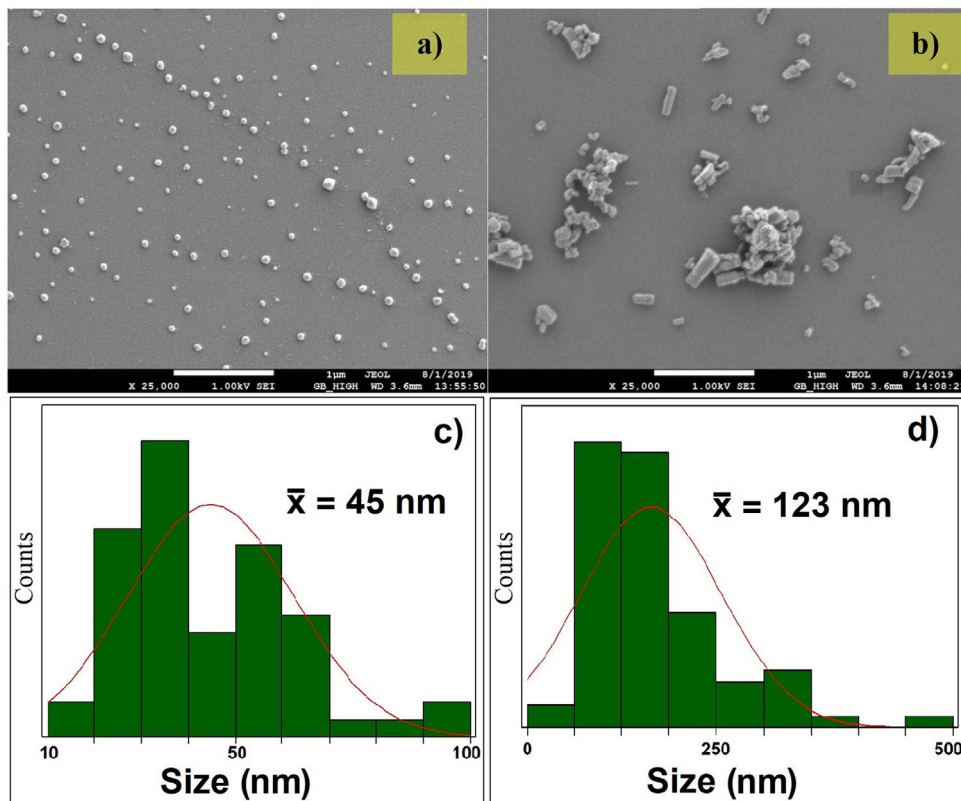


Fig. 2 – Images obtained by FE-SEM of particles of (a) ZnO and (b) AZO; size distribution for (c) ZnO particles and (d) AZO particles.

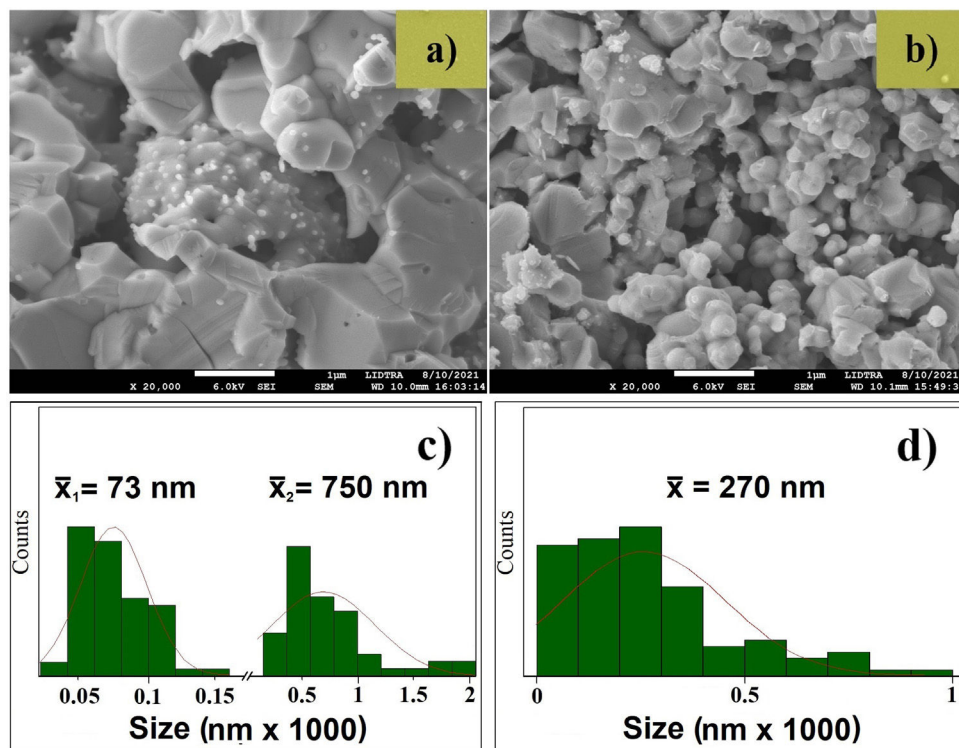


Fig. 3 – FE-SEM images for (a) ZnO target and (b) AZO target; size distribution for (c) ZnO target and (d) AZO target.

obtained rod-like particles in the range of 1–2 μm [7]. All of these results show that the incorporation of a small amount of Al impacts the morphology of the nanoparticles.

The wide distribution of particle sizes, presented at the bottom of Fig. 2 for both systems, shows the growth in crystallite size calculated for the sintered targets. Considering the presence of particles of 10 nm size and the grain boundary diffusion, it is evident the mass of the smaller particles diffuses better than that of the larger particles, according to a process known as the coarsening of particles [38].

The FE-SEM image of the ZnO target (Fig. 3a) shows grains of different sizes, in the range of 25–1000 nm. The size distribution presented in Fig. 3c evidences the broad range, there are two different grain size, the first mean size centered at 73 ± 24 nm and the second mean size was 750 ± 400 nm. The FE-SEM image of the AZO target is presented in Fig. 3b. It shows grains bigger than 700 nm and smaller than 100 nm. The size distribution presented in Fig. 3d shows a broad range, but the mean size was 270 ± 200 nm. The broad standard deviation for both systems (ZnO and AZO) was obtained due to the different grain sizes seen in the FE-SEM images. Moreover, the morphology, size, and distribution of particle size explain the higher density of the ZnO target compared with the AZO target. The arrangement of particles previous to and during the sintering process was favorable to the greater densification of ZnO, this is evident in the FE-SEM images of the targets.

AZO and ZnO films

Fig. 4 shows the X-ray diffraction patterns of AZO films deposited by sol-gel (A and B), and by sputtering (C, D, and E).

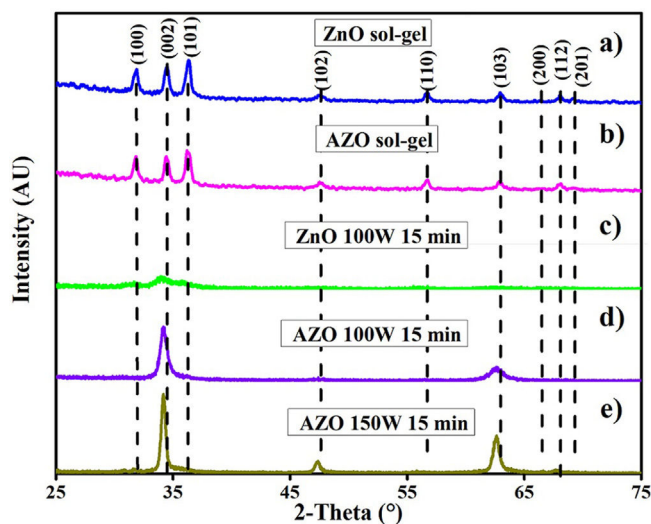


Fig. 4 – X-ray diffraction pattern of films deposited by sol-gel (a) ZnO and (b) AZO; by sputtering (c) ZnO at 100 W, (d) AZO at 100 W, (e) AZO at 150 W.

There is a difference between the X-ray diffraction patterns of the films deposited using the two techniques.

The X-ray diffraction patterns show a random orientation of the crystalline structure according to PDF 36-1451 for the films deposited by sol-gel. For the films deposited by sputtering at 100 W and 150 W, the X-ray diffraction patterns show a pronounced peak around an angle of 34 degrees, indicating a preferential orientation to the (002) plane. The absence

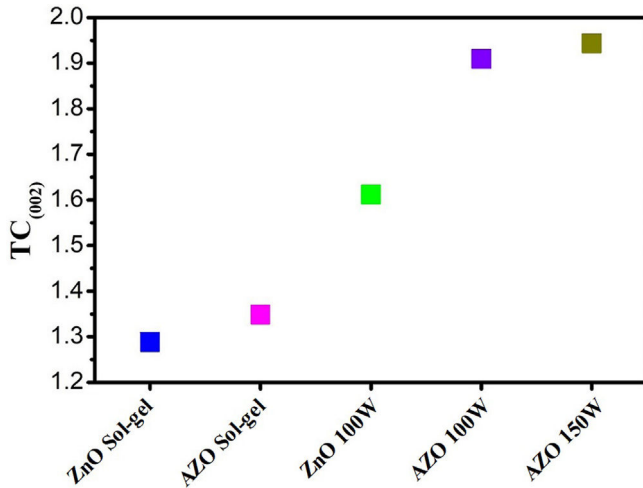


Fig. 5 – Texture coefficient calculated using the Harris equation for the thin films deposited by sol-gel and sputtering.

of additional peaks in the AZO thin film X-ray diffractograms indicates that no other impurities, such as aluminum oxide, were formed.

The FE-SEM images show the early effect of the addition of aluminum on the morphology of the particles, but there is no presence of Al_2O_3 or any other secondary phase in the X-ray diffraction patterns. This implies that Al gets into the crystalline structure, as previously reported [34,39].

The texture coefficients (TCs) for the thin films are presented in Fig. 5. For thin films deposited by sputtering, the TC shows a preferential orientation to the (002) plane; however, thin films deposited by sol-gel present a low orientation in the same plane.

The preferential orientation presented for the thin films deposited by sputtering can be explained by the drift model and the surface energy. The drift model indicates that nucleation at different planes is carried out in the first stages of the deposit of the film, and the nuclei that survive the competition are those that grow fastest on the substrate [35,40]. Furthermore, the (002) plane is the one with the lowest free surface energy, which is why growth in that direction is favored [36]. In addition, for the thin films deposited by sputtering, the values of TC_{hkl} increase with increasing power (Fig. 5).

Table 1 shows the lattice parameters calculated from the X-ray diffraction patterns, crystallite size, and in-plane stress (σ). Considering the biaxial strain model and the elastic stiffness constants for the ZnO, the equation can be written as [41]:

$$\sigma = -233 \frac{C - C_0}{C_0} \text{ (GPa)} \quad (3)$$

where C is the lattice parameter calculated for the film and C_0 is the lattice parameter of reference. The C_0 used as a reference is the lattice parameter calculated for the ZnO synthesized nanoparticles. A negative sign for σ indicates that the films present compressive stress. In contrast, a positive σ for the ZnO and AZO thin films deposited by sol-gel indicate tensile stress. The AZO films deposited by

sol-gel show tensile stress (0.268 GPa), in contrast to the films deposited by sputtering at 100 W, which present compressive stress (-1.520 GPa). The AZO films deposited by the sputtering process at 100 W show tensile stress of -1.52 GPa, a smaller magnitude than that of ZnO films (-2.28 GPa) deposited under the same conditions. This is because the ionic radius of Al^{3+} (0.053 nm) is smaller than that of Zn^{2+} (0.074 nm), considering that according to Singh et al., Al^{3+} enters the crystal lattice at substitutional sites [39]. The compressive stress is also associated with crystal defects caused during the deposition of the films. The compressive stress decreases with the increasing deposition power of the ZnO films doped with Al. This behavior has been reported before for ZnO films [40,42].

The FE-SEM images shown in Fig. 6 are evidence that the films deposited by sol-gel present pores, a characteristic of the sol-gel technique due to the surface tension during the removal of the solvent and the formation of grains during the drying and sintering process. The grain sizes are 26 ± 10 nm and 51 ± 16 nm for the ZnO and AZO, respectively. The addition of Al as $\text{Al}(\text{NO}_3)_3 \cdot 9\text{H}_2\text{O}$ changes the properties of the precursor solution; it can act as an additive, affecting the hydrolysis and condensation by increased water concentration and modifying the grain size in the films [43].

The films deposited by sputtering do not present pores, and the grain size of the AZO films elaborated by the sputtering process at 100 W is 35 ± 12 nm, whereas the film deposited at 150 W has an average grain size of 58 ± 13 nm. Both are smaller than the grain size of the undoped ZnO films deposited by sputtering (66 ± 33 nm). The large standard deviation of the grain size distribution of ZnO films deposited by sputtering indicates the presence of small grains (<20 nm) and large grains (>100 nm). This can be seen in the FE-SEM image, and the size of many grains is between 40 and 80 nm. However, the narrower grain size distribution of the AZO films might have been associated with the addition of the dopant under the same deposit conditions. The smaller grain size can be attributed to an effect of Al, because doping can limit the grain growth during film deposition, considering the modeling of grain growth in impure systems [44].

In Fig. 7, the EDS analysis shows that the Al is present in the thin films deposited by both methods. The Al content of approximately 0.8% (Al/Zn) in the films deposited by sol-gel could be due to the measurement technique, considering that EDS is a semi-quantitative analysis, and the Al content obtained is acceptable compared with the calculated in the preparation of the precursor solution.

In the films deposited by sputtering, the aluminum content also increases with the power increase. For both power levels, the content of Al is higher than that of the target. Similar results have previously been reported [45,46]. This can be explained considering that the binding energy is higher for Al–O than for Zn–O, and the collision of the plasma with the substrate promotes the deposition rate for Al over that for Zn [45].

The room temperature photoluminescence spectra of ZnO and AZO films deposited by the sol-gel method are in Fig. 8a. The room temperature photoluminescence spectra of ZnO and AZO films deposited by sputtering are in Fig. 8b. The samples were excited at 325 nm. There are significant bands in the range of 390–398 nm (UV emission); there are also bands in

Table 1 – Properties of films obtained by sputtering and sol-gel. Thickness, crystallite size, in-plane stress, and lattice parameters.

	Power (W)	Thickness (nm)	Crystallite size (nm)	Stress σ (GPa)	Lattice parameters	
					c	a = b
ZnO sol-gel	-	240	16 ± 7	0.447	5.203	3.243
AZO sol-gel	-	315	17 ± 8	0.268	5.207	3.243
ZnO	100	160	12 ± 7	-2.280	5.264	3.271
AZO	100	86	15 ± 7	-1.520	5.247	3.224
AZO	150	172	37 ± 10	-1.386	5.244	3.253
ZnO nanoparticles	-	-	-	-	5.213	3.255

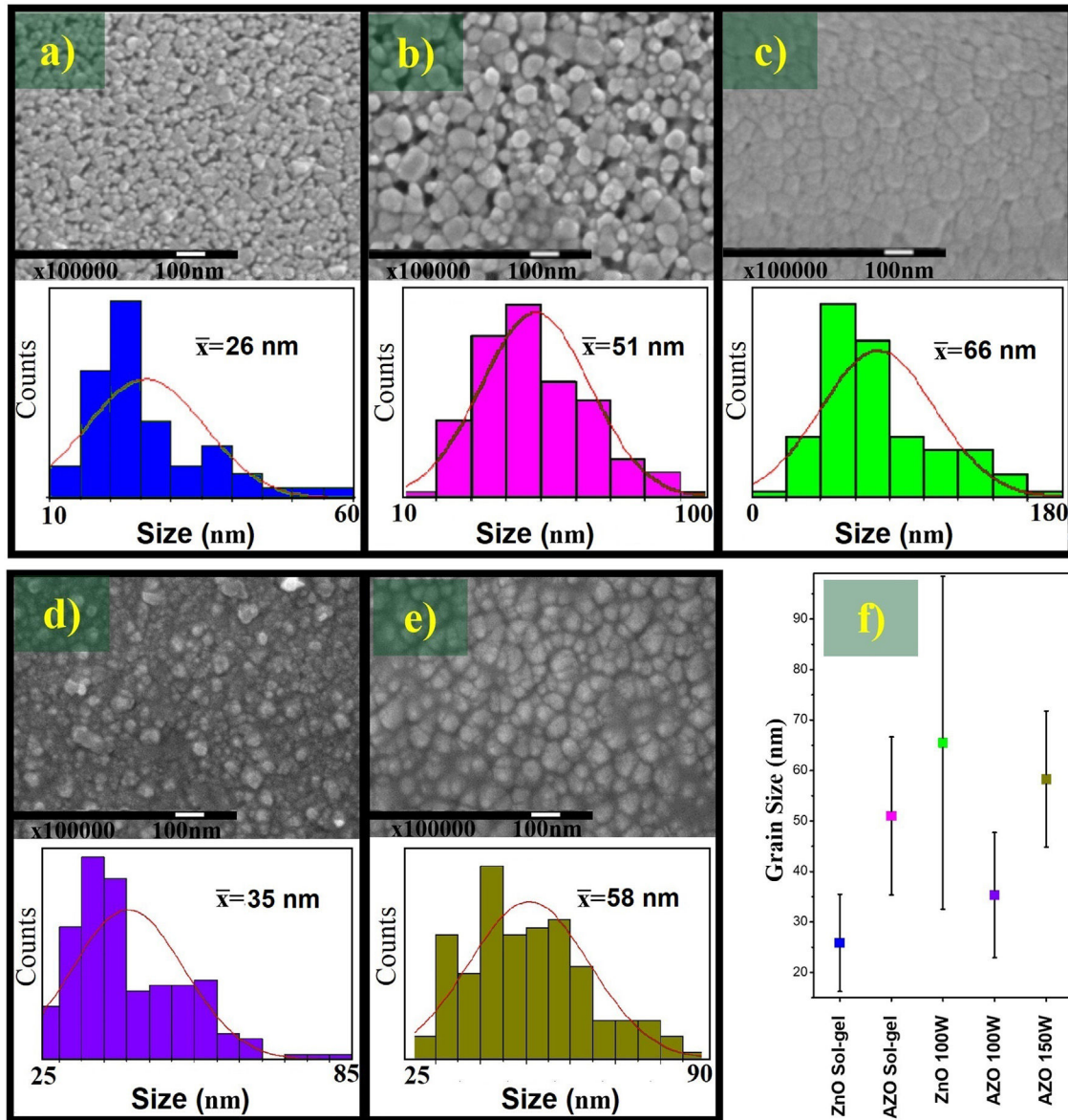


Fig. 6 – FE-SEM images of films deposited by sol-gel (a) ZnO, (b) AZO; sputtering (c) ZnO at 100 W, (d) AZO at 100 W, (e) AZO at 150 W and (f) grain size for thin films deposited by sol-gel and sputtering (bar represents standard deviation).

the range of 410–440 nm (violet emission), 450–470 (blue emission), and 490–560 nm (green emission). The band in the UV emission range at 397.5 nm is related to the recombination of free excitons of ZnO corresponding to the band edge emission

[47]. The bands in the violet region centered at 412, 424, and 440 nm are related to the transition from the conduction band to deep holes trapped above the balance band [47–49]. In the blue region, the bands centered at 449 and 461 nm are related

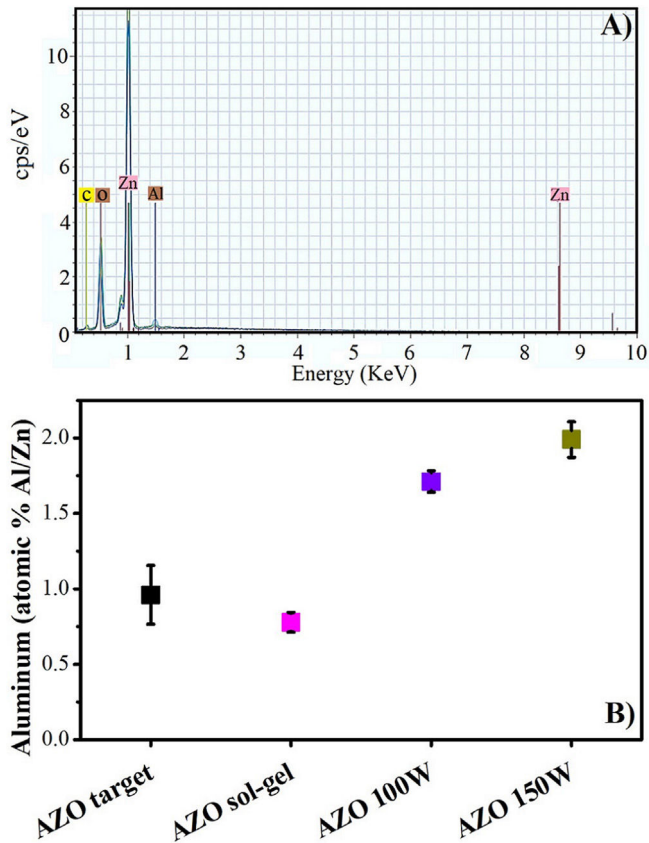


Fig. 7 – (A) Representative EDS of the target of AZO, and (B) EDS analysis for the aluminum content for the thin films and the ZnO in bulk.

to the direct recombination of conduction electrons near the conduction band and holes in the valence band [47–49], the bands could be related to lattice defects caused by compressive strain which leads to zinc and oxygen vacancies and interstitials [50]. The band centered at 486 nm is related to the electronic transition of a donor-level single ionized zinc to an acceptor-level zinc vacancy [47,48,51]. In the green region, the band centered at 530 nm is related to the recombination of photogenerated holes and electron trapped by singly ionized oxygen vacancies [48,49,52].

The spectrum of the films deposited by sol-gel (Fig. 8a) shows a decrease in almost all emissions bands when Al is

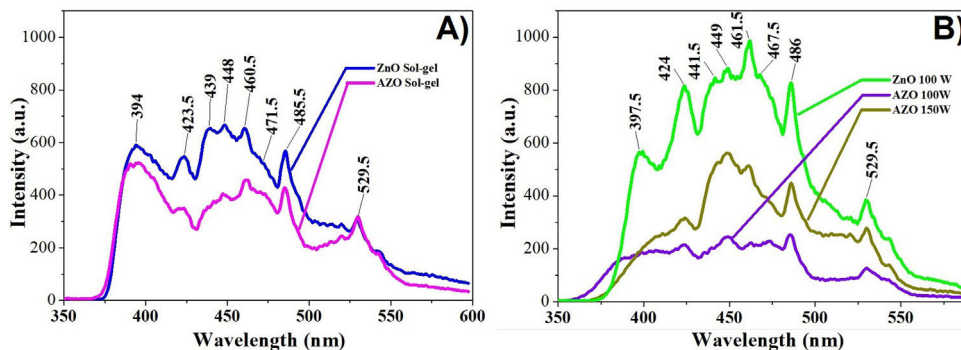


Fig. 8 – Photoluminescence spectrum of ZnO films and AZO films deposited by (a) sol-gel and (b) sputtering.

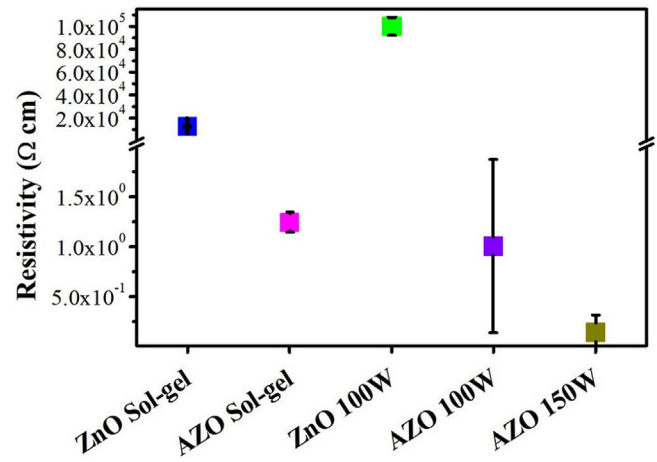


Fig. 9 – Resistivity measured by the four-point probe method for films deposited by sol-gel and sputtering.

added. The band centered at 529.5 nm related to the recombination of photogenerated holes and electrons trapped by single ionized oxygen vacancies remains constant. The band centered around 440 decreases more than the band centered around 460 nm, which means that holes trapped above the balance band decrease more in comparison to other defects.

The photoluminescence spectrum of the films deposited by sputtering (Fig. 8b) shows a large decrease in the emission when Al is added, which means the defects decrease with the addition of the dopant. The band between 440 and 470 nm decreases considerably for the AZO film deposited at 100 W, but increases when the power increases from 100 to 150 W.

An important effect in the AZO films deposited by sputtering is the decrease in the near band emission centered at 397.5 nm. Kouto et al. remark that the presence of multiple peaks indicates multiple defect levels [50].

The resistivity (ρ) is presented in Fig. 9; ρ for the films deposited by sputtering is $1 \Omega \text{ cm}$ for a power level of 100 W and $0.14 \Omega \text{ cm}$ at 150 W. The reduction in resistivity for AZO films with an increase in the power level used in RF magnetron sputtering has previously been reported [40,53,54]. The reduction in resistivity when the power is increased is associated with a higher concentration of Al at substitutional sites and free electrons due to Al ionization [54]. The larger average size of grains in the film deposited by sputtering at 150 W may explain the reduction in resistivity relative to the film deposited at

100 W. The addition of Al as dopant decreases the resistivity fivefold because the Al^{3+} at the substitutional sites acts as a charge carrier donor. The same dopant effect is observed for the films deposited by sol-gel: the resistivity decreases from $2 \times 10^4 \Omega \text{ cm}$ to $1.24 \Omega \text{ cm}$ with the addition of aluminum. AZO thin films deposited by sol-gel show a higher resistivity than AZO films deposited by sputtering at 150 W. This higher resistivity could be associated with the presence of pores and the smaller crystallite size for the sol-gel.

Some authors used AZO targets with relations Al/Zn greater than 1%, Wang et al. deposited films with resistivities on the order of $10^{-2} \Omega \text{ cm}$ using a commercial target having 2% Al_2O_3 (more than 3% Al respect to Zn) for a thickness of 520 nm. The chamber was evacuated to $7 \times 10^{-4} \text{ Pa}$, the power used was 170 W, and the Ar flow was kept constant at 20 sccm [55]. Ayadi et al. fabricated AZO targets with a concentration of Al (Al/Zn) between 1% and 4% in the precursor solution, but the targets had a concentration less than 0.05% and resistivities on the order of 10^{-3} – $10^{-5} \Omega \text{ cm}$. The chamber was evacuated to $3 \times 10^{-4} \text{ Pa}$, and the distance between the target and the substrate was 7.5 cm [34]. Flores et al. presented ZnO films having resistivities greater than $1.3 \Omega \text{ cm}$ and a thickness of 117 nm of thickness. They used a similar configuration that the one used in this work. The power level used was 200 W, 50 sccm of Ar flow, and 15 min of deposition time [40]. In accordance with the results, low Ar flows and higher power densities could be explored to reduce the resistivity and enhance other parameters of interest

However, we can attribute the decreasing resistivity of the thin films deposited by sputtering to diverse factors:

- 1) In thin ZnO films, the number of grain boundaries decreases when the deposition power increases.
- 2) The grain boundaries may be considered as defects and can act as recombination centers. The addition of aluminum as dopant reduces the number of defects, and the stress in the ZnO leads to better crystallinity, which contributes to increased electrical conductivity.
- 3) Additionally, there is a significant increase in the concentration of Al in films as the deposition power increases, implying an increase in the concentration of carriers, which also contributes to a reduction in resistivity.

The resistivity decrease due to the power increase is also related to the decrease in the in-plane stress and the larger grain size, TC, and size of crystallites, which are considered macroscopic imperfections [54].

The porosity of the films deposited by sol-gel may be an important issue due to the possibility of having a larger surface area and better interaction between the analyte target and the material. Furthermore, the high orientation to the (002) plane of the films deposited by sputtering may be a significant property because the exposed face may be more specific due to the spacing and atoms exposed. Beitollahi et al. indicated in their studies that surface area, biocompatibility, and electron transfer, among other properties, were relevant parameters to take into account in designing and fabricating sensors and biosensors [17].

The properties of the films deposited by the two methods studied are highly dependent on the process, and the

properties offer different advantages. The sol-gel produces films with higher porosity and random orientation but needs thermal treatment to remove organic precursors, whereas the films deposited by sputtering can be deposited at room temperature with high orientation. This is important when certain flexible substrates, like PET, are used.

The high orientation, homogeneity, small grain size, and low resistivity are relevant properties of films made from ZnO doped with Al and are appropriate for the design of devices like sensors or biosensors, labeled or label-free.

Conclusions

The effect of doping ZnO with Al induces important morphological changes in the ZnO nanoparticles, and these changes range from the semi-spherical particles of ZnO to rod-like particles when ZnO is doped with Al.

The comparative study of the films obtained shows that the preparation targets of ZnO doped with Al through powders derived from the sol-gel process are convenient. The targets do not present secondary phases, and the concentration of the dopant is near its nominal concentration; therefore, they are suitable for obtaining films by sputtering with the required dopant concentration. In this case, the addition of Al allows an appreciable reduction in the electrical resistivity. Highly textured films were obtained on the corning glass in the (002) direction. This texturing result provides an excellent opportunity to explore the sensitivity of the interaction of environmental contaminants with the oriented surface of the ZnO doped with Al. The photoluminescence analysis would allow us to determine and monitor the change in emission bands when the films interact with the analyte. Furthermore, these films may be used as biosensors, due to the changes in the resistance produced by the interaction of the film with the analyte agent.

Conflicts of interest

There are no conflicts of interest to declare.

Funding and acknowledgements

The authors thank UNAM for the support of the UNAM-DGAPA-PAPIME under Grant No. PE104319, and CONACYT under Grants LN2019-299082 and LN2020-314848. The use of the facilities of the experimental infrastructure of LIDTRA is acknowledged. F.G.S. thanks CONACYT for the scholarship to carry out his Ph.D. studies. We thank Ph.D. Rebeca Castanedo Pérez for the use of the Loretta-6P equipment, model MCP-T600 for electrical resistivity measurements. Also, we thank Carlos Alberto Ávila Herrera for the technical support and the use of the RF-sputtering equipment.

REFERENCES

- [1] Z.C. Feng, *Handbook of Zinc Oxide and Related Materials: Volume Two, Devices and Nano-engineering*, CRC Press, 2012.

- [2] C.F. Klingshirn, A. Waag, A. Hoffmann, et al., in: S.S.B. Media (Ed.), *Zinc Oxide: From Fundamental Properties Towards Novel Applications*, Springer, 2010.
- [3] M. Willander, *Zinc Oxide Nanostructures: Advances and Applications*, CRC Press, 2014.
- [4] M. Wang, K.E. Lee, S.H. Hahn, et al., Optical and photoluminescent properties of sol-gel Al-doped ZnO thin films, *Mater. Lett.* 61 (4–5) (2007) 1118–1121, <http://dx.doi.org/10.1016/j.matlet.2006.06.065>.
- [5] V.L.R. Pullagurala, I.O. Adisa, S. Rawat, et al., Finding the conditions for the beneficial use of ZnO nanoparticles towards plants-A review, *Environ. Pollut.* 241 (2018) 1175–1181, <http://dx.doi.org/10.1016/j.envpol.2018.06.036>.
- [6] S. Hosseini, *Green synthesis of agricultural waste biomass-assisted metal and metal oxide nanostructures and their applications: a review*, in: 16th National Chemistry Conference of Payame Noor University, Karaj, Iran, 2020.
- [7] P. Rameshkumar, V. Balaprakash, P. Gowrisankar, Preparation and characterization of alumina doped zinc oxide (Al-ZnO) nanoparticles by co-precipitation method for photocatalytic activity on dyes, *NOVYI MIR Res. J.* 5 (9) (2020).
- [8] Y. Sun, L. Chen, Y. Bao, et al., The applications of morphology controlled ZnO in catalysis, *Catalysts* 6 (12) (2016) 188, <http://dx.doi.org/10.3390/catal6120188>.
- [9] P.S.K.N.K. Bhat, P. Nagaraju, Fabrication of ultrasensitive hexagonal disc structured ZnO thin film sensor to trace nitric oxide, *J. Asian Ceram. Soc.* 9 (1) (2021) 96–105, <http://dx.doi.org/10.1080/21870764.2020.1848036>.
- [10] H. Dong, Y. Liu, J. Lu, et al., Single-crystalline tower-like ZnO microrod UV lasers, *J. Mater. Chem. C* 1 (2) (2013) 202–206, <http://dx.doi.org/10.1039/C2TC00070A>.
- [11] X. Fang, Y. Bando, U.K. Gautam, et al., ZnO and ZnS nanostructures: ultraviolet-light emitters, lasers, and sensors, *Crit. Rev. Solid State Mater. Sci.* 34 (3–4) (2009) 190–223, <http://dx.doi.org/10.1080/10408430903245393>.
- [12] A.J. Gimenez, G. Luna-Bárceñas, I.C. Sanchez, et al., Paper-based ZnO oxygen sensor, *IEEE Sens. J.* 15 (2) (2015) 1246–1251, <http://dx.doi.org/10.1109/JSEN.2014.2361780>.
- [13] A. Kolodziejczak-Radzimska, T. Jesionowski, Zinc oxide—from synthesis to application: a review, *Materials* 7 (4) (2014) 2833–2881, <http://dx.doi.org/10.3390/ma7042833>.
- [14] B. Liu, C. Wang, S. Bazri, et al., Optical properties and thermal stability evaluation of solar absorbers enhanced by nanostructured selective coating films, *Powder Technol.* (2020), <http://dx.doi.org/10.1016/j.powtec.2020.09.040>.
- [15] C.N. Wang, Y.L. Li, F.L. Gong, et al., Advances in doped ZnO nanostructures for gas sensor, *Chem. Rec.* 20 (12) (2020) 1553–1567, <http://dx.doi.org/10.1002/tcr.202000088>.
- [16] S. Bagyalakshmi, A. Sivakami, K. Balamurugan, A ZnO nanorods based enzymatic glucose biosensor by immobilization of glucose oxidase on a chitosan film, *Obes. Med.* 18 (2020) 100229, <http://dx.doi.org/10.1016/j.obmed.2020.100229>.
- [17] H. Beitollahi, S. Tajik, F.G. Nejad, et al., Recent advances in ZnO nanostructure-based electrochemical sensors and biosensors, *J. Mater. Chem. B* 8 (27) (2020) 5826–5844, <http://dx.doi.org/10.1039/D0TB00569J>.
- [18] Y. Lei, X. Yan, J. Zhao, et al., Improved glucose electrochemical biosensor by appropriate immobilization of nano-ZnO, *Colloids Surf. B: Biointerfaces* 82 (1) (2011) 168–172, <http://dx.doi.org/10.1016/j.colsurfb.2010.08.034>.
- [19] A. Wei, X.W. Sun, J. Wang, et al., Enzymatic glucose biosensor based on ZnO nanorod array grown by hydrothermal decomposition, *Appl. Phys. Lett.* 89 (12) (2006) 123902, <http://dx.doi.org/10.1063/1.2356307>.
- [20] G. Villasana-Ponce, F. Chalé-Lara, J. Olarte Villamizar, et al., ZnO thin film as non-enzymatic glucose sensor in an alkaline solution, *Superficies y vacío* 32 (2019) 22–26.
- [21] H.Y. Yue, H.J. Zhang, S. Huang, et al., Highly sensitive and selective dopamine biosensor using Au nanoparticles-ZnO nanocone arrays/graphene foam electrode, *Mater. Sci. Eng. C* 108 (2020) 110490, <http://dx.doi.org/10.1016/j.msec.2019.110490>.
- [22] B. Ismail, M. Abaab, B. Rezig, Structural and electrical properties of ZnO films prepared by screen printing technique, *Thin Solid Films* 383 (1–2) (2001) 92–94, [http://dx.doi.org/10.1016/S0040-6090\(00\)01787-9](http://dx.doi.org/10.1016/S0040-6090(00)01787-9).
- [23] Q. Qi, T. Zhang, Q. Yu, et al., Properties of humidity sensing ZnO nanorods-base sensor fabricated by screen-printing, *Sens. Actuators B: Chem.* 133 (2) (2008) 638–643, <http://dx.doi.org/10.1016/j.snb.2008.03.035>.
- [24] R.A. Zargar, S. Chackrabarti, S. Joseph, et al., Synthesis and characterization of screen printed ZnO films for solar cell applications, *Optik* 126 (23) (2015) 4171–4174, <http://dx.doi.org/10.1016/j.ijleo.2015.08.115>, 2015/12/01/.
- [25] A. Ramadhan, N.L.W. Septiani, W.A.E. Prabowo, et al. (Eds.), *Temperature Effect of Chemical Bath Deposition (CBD) to Fabrication and Characterization of Zinc Oxide Nanorods Thin Films Based Gas Sensing: Ethanol*, *Journal of Physics: Conference Series*. IOP Publishing, 2020.
- [26] J. Villafuerte, F. Donatini, J. Kioseoglou, et al., Zinc vacancy-hydrogen complexes as major defects in ZnO nanowires grown by chemical bath deposition, *J. Phys. Chem. C* 124 (30) (2020) 16652–16662, <http://dx.doi.org/10.1021/acs.jpcc.0c04264>.
- [27] S. Vipul, P.D. Amit, Effect of doping concentration on optical and electrical properties of intrinsic n-type ZnO (i-ZnO) and (Cu, Na and K) doped p-type ZnO thin films grown by chemical bath deposition method, *Наносистемы: физика, химия Математика* 11 (4) (2020), <http://dx.doi.org/10.17586/2220-8054-2020-11-4-391-400>.
- [28] M.A. Desai, V. Sharma, M. Prasad, et al., Seed-layer-free deposition of well-oriented ZnO nanorods thin films by SILAR and their photoelectrochemical studies, *Int. J. Hydrogen Energy* 45 (10) (2020) 5783–5792, <http://dx.doi.org/10.1016/j.ijhydene.2019.09.150>.
- [29] I. Linson, S. Padmanabhan, R. Vamadevan, et al. (Eds.), *Characterization of ZnO and Al Doped ZnO Thin Films Prepared by SILAR Method*, *AIP Conference Proceedings*. AIP Publishing LLC, 2020.
- [30] S. Suehiro, K. Horita, A.D. Pramata, et al., Efficient solution route to transparent ZnO semiconductor films using colloidal nanocrystals, *J. Asian Ceram. Soc.* 4 (3) (2016) 319–323, <http://dx.doi.org/10.1016/j.jascerc.2016.06.002>, 2016/09/01.
- [31] P.K. Bhujbal, H.M. Pathan, Temperature dependent studies on radio frequency sputtered Al doped ZnO thin film, *Eng. Sci.* 10 (2020) 58–67, <http://dx.doi.org/10.30919/es8d1003>.
- [32] M. Lee, Y. Park, K. Kim, et al., Influence of sputtering conditions on the properties of aluminum-doped zinc oxide thin film fabricated using a facing target sputtering system, *Thin Solid Films* 703 (2020) 137980, <http://dx.doi.org/10.1016/j.tsf.2020.137980>.
- [33] N. Neves, R. Barros, E. Antunes, et al., Aluminum doped zinc oxide sputtering targets obtained from nanostructured powders: processing and application, *J. Eur. Ceram. Soc.* 32 (16) (2012) 4381–4391, <http://dx.doi.org/10.1016/j.jeurceramsoc.2012.08.007>.
- [34] Z.B. Ayadi, L. El Mir, K. Djessas, et al., The properties of aluminum-doped zinc oxide thin films prepared by rf-magnetron sputtering from nanopowder targets, *Mater. Sci. Eng. C* 28 (5–6) (2008) 613–617, <http://dx.doi.org/10.1016/j.msec.2007.10.006>.
- [35] A. Purohit, S. Chander, A. Sharma, et al., Impact of low temperature annealing on structural, optical, electrical and morphological properties of ZnO thin films grown by RF sputtering for photovoltaic applications, *Opt. Mater.* 49

- (2015) 51–58, <http://dx.doi.org/10.1016/j.optmat.2015.08.021>, 2015/11/01/.
- [36] Y. Wang, W. Tang, L. Zhang, et al., Crystalline size effects on texture coefficient, electrical and optical properties of sputter-deposited Ga-doped ZnO thin films, *J. Mater. Sci.* 31 (2) (2015) 175–181, <http://dx.doi.org/10.1016/j.jmst.2014.11.009>.
- [37] S. Rezabeigy, M. Behboudnia, NJPM.S. Nobari, Growth of ZnO nanorods on glass substrate by chemical bath deposition, *Proc. Mater. Sci.* 11 (2015) 364–369, <http://dx.doi.org/10.1016/j.mspro.2015.11.130>.
- [38] Z. Fang, H. Wang, Densification and grain growth during sintering of nanosized particles, *Int. Mater. Rev.* 53 (6) (2008) 326–352, <http://dx.doi.org/10.1179/174328008X353538>.
- [39] A. Singh, R. Mehra, A. Yoshida, et al., Doping mechanism in aluminum doped zinc oxide films, *J. Appl. Phys.* 95 (7) (2004) 3640–3643, <http://dx.doi.org/10.1063/1.1667259>.
- [40] E. Flores-García, P. González-García, J. González-Hernández, et al., Statistical analysis of sputter parameters on the properties of ZnO thin films deposited by RF sputtering, *J. Electr. Mater.* 47 (9) (2018) 5537–5547, <http://dx.doi.org/10.1007/s11664-018-6422-3>.
- [41] K.H. Ri, Y. Wang, W.L. Zhou, et al., The structural properties of Al doped ZnO films depending on the thickness and their effect on the electrical properties, *Appl. Surf. Sci.* 258 (4) (2011) 1283–1289, <http://dx.doi.org/10.1016/j.apsusc.2011.07.022>.
- [42] X. Zhang, K. Hui, K.S. Hui, et al., Structural and optical characterization of high-quality ZnO thin films deposited by reactive RF magnetron sputtering, *Mater. Res. Bull.* 48 (3) (2013) 1093–1098, <http://dx.doi.org/10.1016/j.materresbull.2012.11.104>.
- [43] Ö. Kesmez, E. Burunkaya, N. Kiraz, et al., Effect of acid, water and alcohol ratios on sol-gel preparation of antireflective amorphous SiO₂ coatings, *J. Non-Cryst. Solids* 357 (16) (2011) 3130–3135, <http://dx.doi.org/10.1016/j.jnoncrsol.2011.05.003>, 2011/08/01.
- [44] A. Michels, C. Krill, H. Ehrhardt, et al., Modelling the influence of grain-size-dependent solute drag on the kinetics of grain growth in nanocrystalline materials, *Acta Mater.* 47 (7) (1999) 2143–2152, [http://dx.doi.org/10.1016/S1359-6454\(99\)00079-8](http://dx.doi.org/10.1016/S1359-6454(99)00079-8).
- [45] M. Chaves, R. Ramos, E. Martins, et al., Al-doping and properties of AZO thin films grown at room temperature: sputtering pressure effect, *Mater. Res.* 22 (2) (2019), <http://dx.doi.org/10.1590/1980-5373-mr-2018-0665>.
- [46] K.C. Park, D.Y. Ma, K.H. Kim, The physical properties of Al-doped zinc oxide films prepared by RF magnetron sputtering, *Thin Solid Films* 305 (1–2) (1997) 201–209, [http://dx.doi.org/10.1016/S0040-6090\(97\)00215-0](http://dx.doi.org/10.1016/S0040-6090(97)00215-0).
- [47] S. Kundu, S. Sain, B. Satpati, et al., Structural interpretation, growth mechanism and optical properties of ZnO nanorods synthesized by a simple wet chemical route, *RSC Adv.* 5 (29) (2015) 23101–23113, <http://dx.doi.org/10.1039/C5RA01152C>.
- [48] B. Maibam, S. Baruah, S. Kumar, Photoluminescence and intrinsic ferromagnetism of Fe doped zinc oxide, *SN Appl. Sci.* 2 (10) (2020) 1–11, <http://dx.doi.org/10.1007/s42452-020-03519-y>.
- [49] K. Bandopadhyay, J. Mitra, Zn interstitials and O vacancies responsible for n-type ZnO: what do the emission spectra reveal? *RSC Adv.* 5 (30) (2015) 23540–23547, <http://dx.doi.org/10.1039/c5ra00355e>.
- [50] V. Koutu, L. Shastri, M. Malik, Effect of NaOH concentration on optical properties of zinc oxide nanoparticles, *Mater. Sci.-Poland* 34 (4) (2016) 819–827, <http://dx.doi.org/10.1515/msp-2016-0119>.
- [51] N. Kumar, A. Katiyar, A. Srivastava, Tuning NBE emission and optical band gap of nanocrystalline ZnO thin films using Fe dopant, *Mater. Today: Proc.* 5 (3) (2018) 9089–9093, <http://dx.doi.org/10.1016/j.matpr.2017.10.025>.
- [52] D. Hernández-Meléndez, E. Salas-Téllez, A. Zavala-Franco, et al., Inhibitory effect of flower-shaped zinc oxide nanostructures on the growth and aflatoxin production of a highly toxigenic strain of *aspergillus flavus* link, *Materials* 11 (8) (2018) 1265, <http://dx.doi.org/10.3390/ma11081265>.
- [53] S. Rahmane, M.A. Djouadi, M.S. Aida, et al., Power and pressure effects upon magnetron sputtered aluminum doped ZnO films properties, *Thin Solid Films* 519 (1) (2010) 5–10, <http://dx.doi.org/10.1016/j.tsf.2010.06.063>.
- [54] A. Spadoni, M. Addonizio, Effect of the RF sputtering power on microstructural, optical and electrical properties of Al doped ZnO thin films, *Thin Solid Films* 589 (2015) 514–520, <http://dx.doi.org/10.1016/j.tsf.2015.06.035>.
- [55] F. Wang, M. Wu, Y. Wang, et al., Influence of thickness and annealing temperature on the electrical, optical and structural properties of AZO thin films, *Vacuum* 89 (2013) 127–131, <http://dx.doi.org/10.1016/j.vacuum.2012.02.040>.